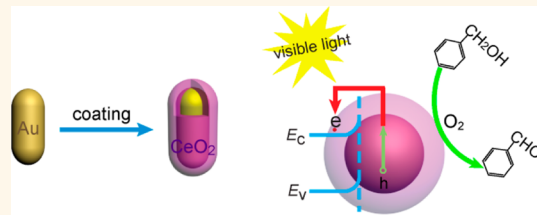


(Gold Core)@(Ceria Shell) Nanostructures for Plasmon-Enhanced Catalytic Reactions under Visible Light

Benxia Li,[†] Ting Gu,[‡] Tian Ming,[†] Junxin Wang,[†] Peng Wang,[§] Jianfang Wang,^{†,*} and Jimmy C. Yu^{‡,*}

[†]Department of Physics and [‡]Department of Chemistry, The Chinese University of Hong Kong, Shatin, Hong Kong SAR China, and [§]Water Desalination and Reuse Center, Biological and Environmental Sciences & Engineering Division, King Abdullah University of Science and Technology, Thuwal, Saudi Arabia

ABSTRACT Driving catalytic reactions with sunlight is an excellent example of sustainable chemistry. A prerequisite of solar-driven catalytic reactions is the development of photocatalysts with high solar-harvesting efficiencies and catalytic activities. Herein, we describe a general approach for uniformly coating ceria on monometallic and bimetallic nanocrystals through heterogeneous nucleation and growth. The method allows for control of the shape, size, and type of the metal core as well as the thickness of the ceria shell. The plasmon shifts of the Au@CeO₂ nanostructures resulting from the switching between Ce(IV) and Ce(III) are observed. The selective oxidation of benzyl alcohol to benzaldehyde, one of the fundamental reactions for organic synthesis, performed under both broad-band and monochromatic light, demonstrates the visible-light-driven catalytic activity and reveals the synergistic effect on the enhanced catalysis of the Au@CeO₂ nanostructures.



KEYWORDS: catalysis · ceria · gold nanocrystals · hot electrons · metal–semiconductor hybrid nanostructures · plasmon resonance

Ceria has attracted wide attention for its broad applications in catalysis,^{1–3} gas sensing,^{4,5} solid oxide fuel cells,⁶ solar cells,⁷ and antioxidant therapy,⁸ due to its capability of adsorbing and releasing oxygen through the Ce(IV)–Ce(III) redox cycle. However, despite the superior performances in CO oxidation^{2,9} and water–gas shift reactions,^{10,11} the catalytic activity of ceria can hardly be driven by light because of two main limiting factors. First, the band gap energy of ceria is ~3.2 eV, which makes CeO₂ only responsive to ultraviolet light. Second, photogenerated carriers in ceria can hardly transport to the surface or interface to participate in chemical reactions owing to their low carrier mobility and therefore short carrier mean free path.^{7,12} To endow CeO₂ with light-driven catalytic capabilities is strongly desired because driving catalytic reactions by solar energy represents a potential type of sustainable chemistry and has been attracting much attention.^{13–15} A prerequisite for driving catalytic reactions with sunlight is the development of photocatalysts with high photon-harvesting efficiencies and catalytic activities in the visible to near-infrared regions.

Gold nanocrystals have recently proven to be promising in harvesting photon energy for chemical reactions due to their extraordinary and tailorabile localized surface plasmon resonance (LSPR) properties.^{16–20} Efficiency enhancements have been demonstrated for visible-light-driven chemical processes by incorporating Au nanocrystals into semiconductors.^{21–25} The enhancements are generally attributed to the LSPR-induced light focusing in the vicinity of Au nanocrystals and/or plasmon-induced charge transfer from Au nanocrystals to semiconductors. In this regard, intimate integration of ceria with Au nanocrystals at the nanoscale is expected to enable ceria to be activated by light in the visible to near-infrared region and function as a photocatalyst for desired chemical reactions. Indeed, CeO₂ loaded with Au nanoparticles has been found to be the most efficient among various (plasmonic Au)–(metal oxide) composites for the mineralization of organic acids in aqueous solutions under visible light illumination.^{26,27} Au/CeO₂ composite prepared by a multistep photodeposition exhibits a high activity in selective oxidation of alcohols.²³ These previous

*Address correspondence to jfwang@phy.cuhk.edu.hk, jimyu@cuhk.edu.hk.

Received for review April 28, 2014 and accepted July 16, 2014.

Published online July 16, 2014
10.1021/nn502303h

© 2014 American Chemical Society

studies demonstrate unambiguously that visible light response can be introduced to CeO_2 by combining plasmonic Au nanocrystals. However, the hybrid structures in these studies are all based on the random adhesion of Au nanoparticles on ceria.^{23,28} To combine plasmonic metal nanocrystals with ceria in a well-defined geometry will be highly desirable to better understand the light absorption, charge carrier excitation, and transfer in the promotion of chemical reactions. Such understanding will be important and helpful for further designing hybrid nanostructures with optimal activities and selectivities.

In this work, we developed a general approach for the preparation of unprecedented (plasmonic metal nanocrystal core)@(CeO_2 shell) nanostructures through heterogeneous nucleation and growth. The core@shell design can potentially improve photocatalytic performance by making full use of the LSPR-induced light focusing for enhanced light absorption as well as the metal nanocrystal surface for charge transfer.^{29–31} It can also protect the metal nanocrystal core from chemical etching, reshaping, and aggregation. Moreover, the size, shape, and composition of the metal nanocrystal core can be finely adjusted to tailor the LSPR properties for efficient light harvesting. We realized uniform coating of CeO_2 on Au nanospheres, Au nanorods, bimetallic Au@Pd, and Au@Pt nanorods to produce nearly monodisperse core@shell nanostructures. The plasmon wavelengths of the (Au core)@(CeO_2 shell) nanostructures can be varied from the visible to the near-infrared region. We found that the Au nanocrystal core can readily sense the oxidation state of Ce in the shell through plasmon shifts. We further demonstrated that the (Au core)@(CeO_2 shell) nanostructures are an attractive type of photocatalysts for the selective oxidation of benzyl alcohol to benzaldehyde with O_2 , one of the fundamental reactions in organic synthesis,³² under both broad-band and monochromatic visible light. The conversion rates obtained with our core@shell nanostructures are superior to those demonstrated in most of the previous studies for the same reaction carried out under different visible light sources with catalysts made of different noble metals or metal oxides. The visible-light-driven catalytic activity of the nanostructures is derived from the synergistic effect between the plasmonic metal core and the catalytic CeO_2 shell.

RESULTS AND DISCUSSION

Monometallic Au nanospheres, Au nanorods, bimetallic Au@Pd, and Au@Pt nanorods that were stabilized with cetyltrimethylammonium bromide (CTAB) in aqueous solutions were employed as the cores to prepare the core@shell nanostructures (Figure 1a). Two Au nanosphere samples were used. Their average diameters are 54 ± 3 and 135 ± 7 nm, respectively. In aqueous solutions, the two nanosphere samples have

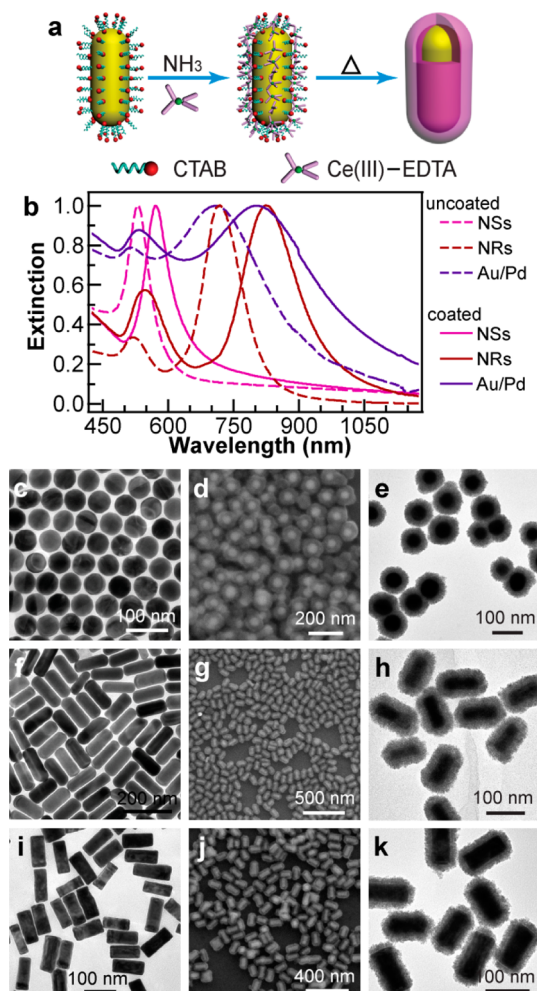


Figure 1. Coating of CeO_2 on metal nanocrystals. (a) Schematic illustrating the preparation of (metal core)@(CeO_2 shell) nanostructures. (b) Normalized extinction spectra of one Au nanosphere sample (AuNS530), one Au nanorod sample (AuNR715), and one Au@Pd nanorod sample before and after CeO_2 coating. (c–k) Transmission electron microscopy (TEM, uncoated, left column), scanning electron microscopy (SEM, coated, middle column), and TEM (coated, right column) images: (c–e) for the Au nanosphere sample; (f–h) for the Au nanorod sample; (i–k) for the Au@Pd nanorod sample. All of the core@shell nanostructure samples are as-prepared without calcination.

ensemble plasmon peaks at 530 and 591 nm. They are therefore denoted as AuNS530 and AuNS591. Four Au nanorod samples were employed. Their average lengths/diameters are $(39 \pm 3 \text{ nm})/(99 \pm 8 \text{ nm})$, $(30 \pm 2 \text{ nm})/(89 \pm 7 \text{ nm})$, $(20 \pm 2 \text{ nm})/(79 \pm 6 \text{ nm})$, and $(15 \pm 2 \text{ nm})/(70 \pm 8 \text{ nm})$, respectively. In aqueous solutions, their ensemble longitudinal plasmon wavelengths are 715, 750, 804, and 865 nm, and therefore, they are named AuNR715, AuNR750, AuNR804, and AuNR865, respectively. For the coating, $\text{Ce}(\text{NO}_3)_3$, ethylenediaminetetraacetic acid (EDTA), and a proper amount of ammonia were added to the CTAB-stabilized metal nanocrystal solution, where the formation of Ce(III)–EDTA complex ions prevents the rapid hydrolysis of Ce^{3+} ions.³³ The negatively charged complex ions

readily adsorbed to the positively charged metal nanocrystal surface.³⁴ Upon heating at 90 °C, the complex ions hydrolyzed and condensed slowly, which was accompanied by oxidation by dissolved O₂ to realize preferential heterogeneous nucleation and growth of the CeO₂ shell around the metal nanocrystals. We note that oxidation of Ce(III) species to produce CeO₂ under similar conditions has also been reported before.^{35,36}

The representative core@shell nanostructures with Au nanospheres, Au nanorods, Au@Pd, and Au@Pt nanorods as the cores are shown in Figure 1 and Figures S1–S3 in the Supporting Information. The CeO₂ shell in all of the core@shell nanostructures is relatively uniform. After CeO₂ coating, the plasmon peaks of the metal nanocrystal samples red shift due to the increase in the refractive index of the surrounding medium.^{34,37} The shapes of the core@shell nanostructures resemble those of their corresponding cores except that the overall sizes become larger. The thickness of the CeO₂ shell can be varied in the range of 6–25 nm by controlling the reaction time or the amount of Ce(NO₃)₃ (Supporting Information Figures S4 and S5). When CeO₂ was coated on Au nanorods, the longitudinal plasmon wavelength and the CeO₂ shell thickness of the core@shell nanostructure were seen to vary largely in the reaction time up to 5 h but change only slightly when the coating time was extended to be longer than 5 h (Supporting Information Figure S4). The CeO₂ coating kinetics was found to be mainly controlled by the Ce³⁺/EDTA molar ratio and the amount of ammonia (Supporting Information Figures S6 and S7). The hydrolysis and condensation of Ce³⁺ to CeO₂ becomes faster as the Ce³⁺/EDTA molar ratio in the solution is increased, with the other reaction parameters kept unchanged. When the Ce³⁺/EDTA molar ratio was adjusted to 0.5, no CeO₂ formed in the solution because of the strong chelation of EDTA to Ce³⁺. In contrast, when the Ce³⁺/EDTA molar ratio was increased to 2, a mixture of CeO₂ nanoparticles and uncoated Au nanorods was obtained. This result is attributed to the insufficient chelating capability of EDTA under this condition. The insufficient chelation makes the hydrolysis and condensation of Ce³⁺ so fast that CeO₂ precipitates from the solution through homogeneous nucleation. The amount of ammonia in the coating solution also plays an important role in the formation of the CeO₂ shell. When a small amount of the concentrated ammonia (<0.08 vol %) was added to the solution, nearly no CeO₂ nanoparticles were formed on the surface of the Au nanorods. In contrast, when the amount of the concentrated ammonia was increased to 0.2 vol %, (Au nanorod core)@CeO₂ nanostructures were produced, together with a number of isolated CeO₂ nanoparticles. Therefore, an excess amount of ammonia makes the hydrolysis and condensation of Ce³⁺ so fast that both heterogeneous

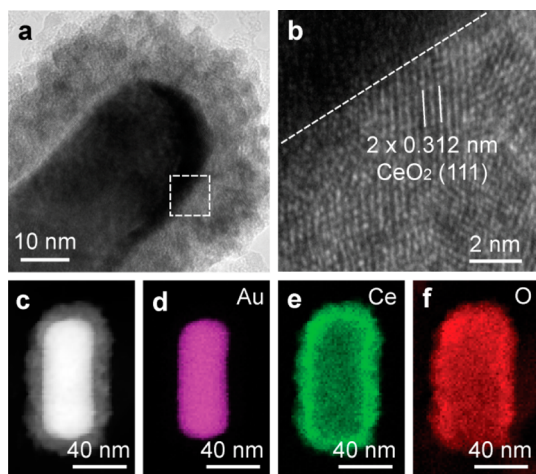


Figure 2. Crystalline structure and composition of the as-prepared (Au nanorod core)@CeO₂ shell nanostructures. (a) TEM image taken at the end of a single core@shell nanostructure. (b) HRTEM image recorded from the area marked with a box in (a). The dashed line indicates the interface between Au and CeO₂. (c) High-angle annular dark-field scanning transmission electron microscopy (HAADF-STEM) image of a single nanostructure. (d–f) Elemental maps of Au, Ce, and O, respectively, on the nanostructure shown in (c). The Au nanorod sample used for coating is AuNR715.

and homogeneous nucleation and growth occur simultaneously in the solution.

To examine the structure and composition of the (metal core)@CeO₂ shell nanostructures, we performed high-resolution transmission electron microscopy (HRTEM) and elemental mapping on the representative individual nanostructures (Figure 2, Supporting Information Figures S8 and S9). According to the HRTEM images, the shells are composed of CeO₂ nanoparticles that are ~5 nm in size. The nanoparticles are loosely bound together. They are crystalline with an interplanar spacing of 0.312 nm, which corresponds to the (111) plane of the cubic CeO₂ phase. The lattice spacing of the Au nanocrystal core cannot be resolved due to the encapsulation of the CeO₂ shell. The elemental distributions in the (Au nanorod core)@CeO₂ shell (Figure 2c–f), (Au nanorod core)@Pd shell)@CeO₂ shell (Supporting Information Figure S8), and (Au nanorod core)@Pt shell)@CeO₂ shell (Supporting Information Figure S9) nanostructures are revealed by elemental mapping. The X-ray diffraction (XRD) pattern (Figure 3) of the (Au core)@CeO₂ shell nanostructures presents two sets of diffraction peaks. One is assigned to the cubic CeO₂ phase (JCPDS No. 04-0593) and the other to the cubic Au phase (JCPDS No. 04-0784). The diffraction peaks of the Au core are sharp and intense, while those of the CeO₂ shell are broad and weak, suggesting the small size of the CeO₂ crystallites. The crystallinity of CeO₂ in the core@shell nanostructures is increased slightly after calcination.

The switching between the Ce(IV) and Ce(III) states has been widely thought to be the underlying reason for many catalytic and biomedical applications of ceria nanostructures.^{1–3,8} A high Ce(III) concentration

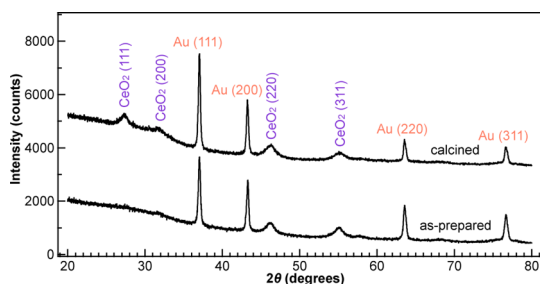


Figure 3. XRD patterns of the as-prepared and calcined (AuNR715 core)@CeO₂ shell nanostructure samples.

can give ceria nanostructures an outstanding catalytic capability to reversibly release/store oxygen from/into them through the creation of oxygen vacancies. Therefore, a number of studies have been devoted to the investigation of the reducibility of ceria nanostructures.^{38–40} However, to directly probe the redox states of ceria nanostructures has remained difficult, owing to the complicated intertwined redox and diffusion processes between the Ce(IV) and Ce(III) states.^{41,42} In our study, we observed distinct plasmon shifts on the (Au core)@CeO₂ shell nanostructures upon the introduction of a reducing or oxidizing agent. For a typical as-prepared (Au nanorod core)@CeO₂ shell nanostructure sample, its longitudinal plasmon peak was at 825 nm (Figure 4a and Supporting Information Figure S10). Upon the addition of NaBH₄, the longitudinal plasmon peak blue shifted to 780 nm. When H₂O₂ was subsequently applied, the longitudinal plasmon peak shifted back to its original position at 825 nm. The redox switching between the Ce(IV) and Ce(III) states is also confirmed by the changes of the absorption spectra when H₂O₂ and NaBH₄ are sequentially added into an aqueous Ce(NO₃)₃ solution (Supporting Information Figure S11a). In contrast, plasmon shifts were not observed for the corresponding uncoated Au nanorod sample upon the addition of NaBH₄ or H₂O₂ (Supporting Information Figure S11b). Similar plasmon shifts have been observed before in Au/CeO₂ films, which display blue shifts in the peak position for reducing gases, such as H₂ and CO, and red shifts for oxidizing gases, such as NO₂, at a temperature of 500 °C.^{4,5}

The changes of the Ce valence state in the CeO₂ shell upon the addition of NaBH₄ or H₂O₂ were ascertained by X-ray photoelectron spectroscopy (XPS) for the same core@shell nanostructure sample used in the plasmon shift measurements (Figure 4b–d and Supporting Information Figure S12). The Ce 3d spectra were fitted with 10 peaks, as described in previous studies.^{41,42} The obtained binding energy and area fraction of each peak are listed in Table S1 of the Supporting Information. The Ce(III) ratios relative to the total amounts of Ce are estimated to be 23.9, 32.9, and 26.6% for the as-prepared, reduced, and reoxidized core@shell nanostructure samples, respectively,

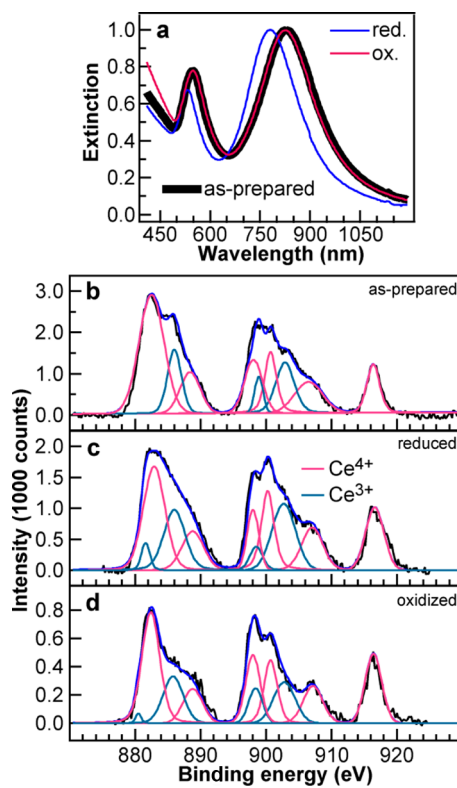


Figure 4. Plasmon shifts and XPS spectra of an as-prepared (Au nanorod core)@CeO₂ shell nanostructure sample under the different redox conditions. (a) Normalized extinction spectra of the core@shell nanostructure sample. (b–d) XPS Ce 3d spectra fitted with 10 peaks for the as-prepared, reduced, and oxidized nanostructure sample, respectively. The Au nanorod sample used for coating is AuNR715.

using the reported equation.^{41,42} It is noted that CeO₂ nanocrystals containing a similar fraction of Ce(III) have also been reported previously.⁴³ The presence of Ce(III) in the as-prepared nanostructure sample is attributed to the small size of the ceria particles, which possess a high concentration of defects, as also suggested by Raman spectra (Supporting Information Figure S13). The Raman spectra are dominated by the F_{2g} mode of the cubic CeO₂ structure around 445 cm^{−1}, which is attributed to a symmetrical stretching mode of the Ce–O₈ vibrational unit. CeO₂ in the core@shell nanostructures gives a very broad peak around 445 cm^{−1}. This can be explained by the inhomogeneous strain broadening associated with the dispersion in the particle size and by phonon confinement. The small CeO₂ particle size is consistent with the XRD and TEM characterizations. The defect concentrations in the CeO₂ shell for the as-prepared and calcined core@shell nanostructure samples are calculated to be 2.82×10^{27} and $1.43 \times 10^{27} \text{ m}^{-3}$, respectively, using the equations provided in previous studies.^{44,45} The treatment with NaBH₄ generates more Ce(III) species in the CeO₂ shell. The amount of the generated Ce(III) by NaBH₄ reduction might be underestimated because some of Ce(III) species can be oxidized when the sample was

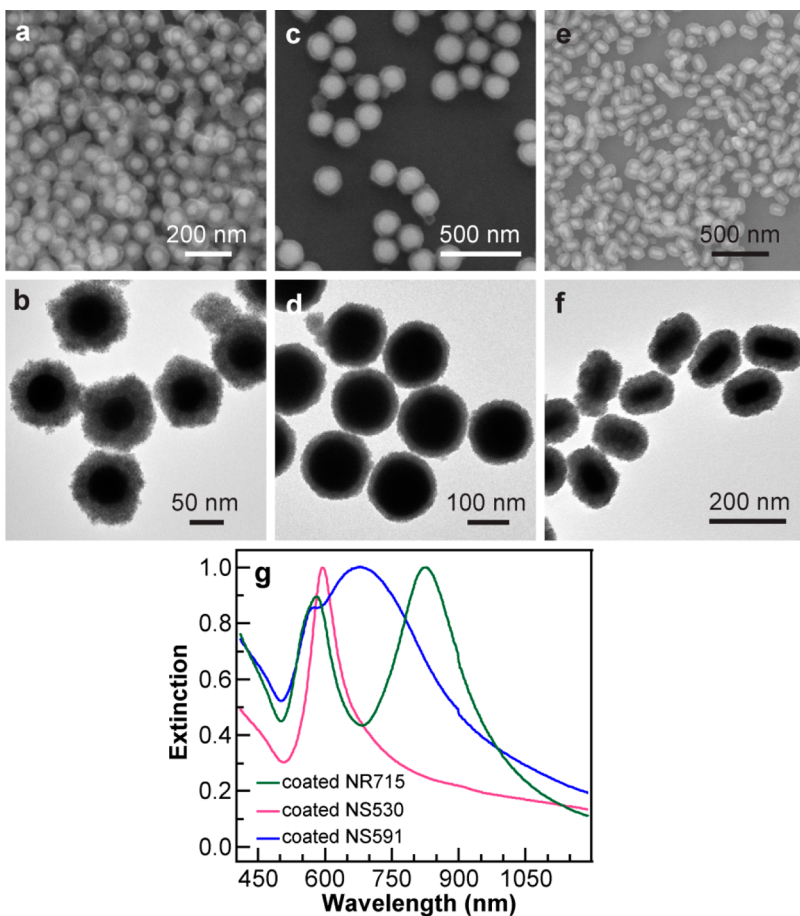


Figure 5. Calcined core@shell nanostructure samples. On the top row are the SEM images, and on the second row are the TEM images. (a,b) (AuNS530 core)@(CeO_2 shell) nanostructures. (c,d) (AuNS591 core)@(CeO_2 shell) nanostructures. (e,f) (AuNR715 core)@(CeO_2 shell) nanostructures. (g) Normalized extinction spectra of the three nanostructure samples.

prepared in air for the XPS measurements. The Ce(III) content is decreased to 26.6% after the reoxidation with H_2O_2 . The variation trend in the amount of Ce(III) species obtained from the XPS measurements is consistent with the plasmon shifts described above. The switching between the Ce(IV) and Ce(III) states probably causes a reversible change in the average refractive index of the CeO_2 shell. The average index is decreased when more Ce(III) species are generated through reduction, which induces a blue shift in the longitudinal plasmon peak.^{34,37} Our results therefore point out a convenient way for monitoring the redox states of ceria nanostructures by measuring the plasmon shifts of metal nanocrystals.

To examine the photocatalytic activity of the (Au core)@(CeO_2 shell) nanostructures under visible light, the nanostructure catalysts were calcined at 350 °C for 3 h to remove the CTAB molecules remaining in the CeO_2 shell. After calcination, the shape and dispersibility remained nearly unchanged (Figure 5). The plasmon peaks of the (AuNS530 core)@(CeO_2 shell) and (AuNS591 core)@(CeO_2 shell) nanostructure samples red-shifted from 571 to 595 nm and from 670 to 680 nm, respectively. The longitudinal plasmon peak

of the (AuNR715 core)@(CeO_2 shell) nanostructure sample remained at the same spectral position of 825 nm. Selective oxidation of benzyl alcohol to benzaldehyde with O_2 in acetonitrile was chosen as a model reaction (Figure 6a). The reaction was carried out under either the broad-band light ($\lambda > 420$ nm; optical power = 5.6 W; spot size = 3.1 cm^2 ; electric power = 250 W) from a Xe lamp or a monochromatic 671 nm laser (optical power = 1.1 W; spot size = 1.8 cm^2). The Xe lamp had the maximal emission intensity in the range from 500 to 600 nm (Supporting Information Figure S14). The (AuNS530 core)@(CeO_2 shell) and (AuNS591 core)@(CeO_2 shell) nanostructure samples were used as the catalysts under the Xe lamp and laser, respectively. The amount of each catalyst was measured by inductively coupled plasma atomic emission spectroscopy (ICP-AES) (Supporting Information Table S2). The conversion to benzaldehyde increases in amount with the reaction time (Supporting Information Figure S15). The time-dependent conversion can be fitted according to pseudo-first-order kinetics since O_2 is in excess for the reaction. The conversion yields after 8 h of reaction under the Xe lamp are listed in Table S3 of the Supporting Information and plotted in Figure 6b for

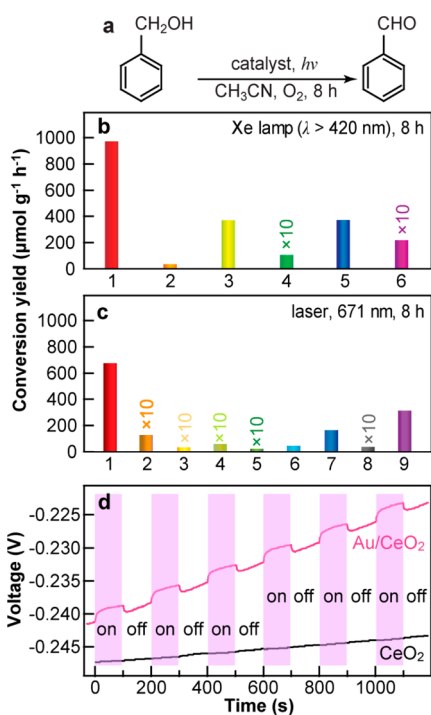


Figure 6. Plasmon-enhanced catalytic reactions and open-circuit voltage measurements. (a) Catalytic reaction. (b) Conversion rates of benzaldehyde under the Xe lamp over the different catalysts: 1, calcined AuNS530@CeO₂; 2, uncalcined AuNS530@CeO₂; 3, calcined CeO₂; 4, uncoated AuNS530; 5, mixture of AuNS530 and calcined CeO₂; 6, calcined AuNS530@SiO₂. (c) Conversion rates under the 671 nm laser or in dark over the different catalysts: 1, calcined AuNS591@CeO₂; 2, uncalcined AuNS591@CeO₂; 3, calcined CeO₂; 4, uncoated AuNS591; 5, mixture of AuNS591 and calcined CeO₂; 6, calcined AuNR664@SiO₂; 7, calcined AuNR715@CeO₂; 8, calcined AuNS591@CeO₂ at room temperature in dark; 9, calcined AuNS591@CeO₂ at 38 °C in dark. (d) Open-circuit voltage curves of the calcined AuNS591@CeO₂ and CeO₂ nanostructure samples under the illumination of the 671 nm laser.

the nanostructure catalyst, together with the other related structures for comparison. The conversion yields have been normalized against the total mass of each catalyst and the reaction time. The calcined (Au NS530 core)@CeO₂ shell) nanostructures deliver the highest conversion rate of 974 $\mu\text{mol}\cdot\text{g}^{-1}\cdot\text{h}^{-1}$, much larger than that of the uncalcined sample, suggesting that the removal of CTAB facilitates charge carrier and mass transfer in the catalyst. For comparison, both the uncoated and silica-coated (see the Supporting Information for the preparation details and Figure S16 for the extinction spectra and TEM images) Au nanosphere samples give negligible conversion in the catalytic reaction, and the other CeO₂-containing catalysts, including pure CeO₂ nanostructures (see the Supporting Information for the preparation details and Figure S17 for the extinction spectrum, TEM images, and XRD patterns) and the mixture of the AuNS530 and CeO₂ nanostructures, are catalytically active with smaller conversion rates. In addition, because in our catalytic reaction oxidation of benzyl alcohol is realized by activated

molecular oxygen instead of photogenerated holes with a high oxidative potential, overoxidation to benzoic acid is too little to be detected. The product selectivities are all close to 100%. This is actually one of the advantages for plasmon-sensitized photocatalytic oxidation.

The normalized conversion yields for the reaction under the 671 nm laser for 8 h are listed in Table S4 of the Supporting Information and plotted in Figure 6c for the different nanostructure catalysts. Similarly to the results of the reaction under the Xe lamp, the calcined (AuNS591 core)@CeO₂ shell) nanostructure sample gives a very high conversion rate of 673 $\mu\text{mol}\cdot\text{g}^{-1}\cdot\text{h}^{-1}$, which is 4 times that obtained over a calcined (Au nanorod core)@CeO₂ shell) nanostructure sample with the longitudinal plasmon peak at 825 nm. In contrast, neither the CeO₂ nanostructures nor the mixture of the AuNS591 and CeO₂ nanostructures are catalytically active under the laser. A (gold nanorod core)@SiO₂ shell) nanostructure sample with the longitudinal plasmon peak at 674 nm (Supporting Information Figure S16) was also tested for comparison. It shows little activity under the 671 nm laser. The conversion rates obtained in our experiments are comparable or much larger than those obtained in most of the previous studies for the same reaction carried out under different visible light sources with catalysts made of different noble metals or metal oxides (Supporting Information Table S5). We have been aware of only one study¹⁸ where a maximal conversion rate at $\sim 8000 \mu\text{mol}\cdot\text{g}^{-1}\cdot\text{h}^{-1}$ was demonstrated under simultaneous visible light illumination and thermal heating (45 °C) with a catalyst made of ZrO₂-supported AuPd alloy nanoparticles that have an optimal Au/Pd molar ratio.

We examined the effect of possibly leached species on the photocatalytic activity, the light power dependence of the activity, and the recyclability with the calcined (AuNS591 core)@CeO₂ shell) nanostructure sample as the catalyst under the 671 nm laser illumination. First, an experiment was performed, where the reaction solution with the catalyst was first illuminated with the laser for 4 h, the catalyst was removed, and then the supernatant without the catalyst was subjected under the laser illumination for another 4 h. The conversion yields before and after the removal of the catalyst were found to be equal. This result suggests that leached Au and Ce species, if they are existent, do not contribute to the photocatalytic activity. Second, the conversion yield was found to show a nonlinear dependence on the optical power of the laser (Supporting Information Table S6). In comparison, a recent study has reported on a superlinear dependence of the photocatalytic reaction rate of excited plasmonic metal nanostructures on the light intensity.⁴⁶ Third, the nanostructure catalysts after 8 h reaction were checked by extinction measurements and TEM imaging (Supporting Information Figure S18).

Their plasmon wavelengths and morphology are well-preserved after reaction. We therefore checked the recyclability of the catalyst by performing six cycles of the reaction. The conversion yields decreased considerably for every next cycle (Supporting Information Table S7). After the fourth cycle, the catalyst was subjected to calcination again. The conversion yields after recalcination in the fifth cycle were increased but were still much smaller than those of the first cycle. We believe that more studies will be required to understand the activity reduction of the recycled core@shell catalyst.

The temperatures of the reaction solution under several typical conditions were measured (Supporting Information Table S8). In addition, the catalytic reaction over the calcined (AuNS591 core)@CeO₂ nanostructures at different temperatures in dark indicates that this nanostructure sample exhibits no catalytic activity at room temperature ($\sim 25^\circ\text{C}$) but a considerable activity at 38°C (Supporting Information Table S4). The temperature of 38°C is the same as that obtained for the reaction solution containing the calcined (AuNS591 core)@CeO₂ nanostructures under the 671 nm laser. The conversion rate at 38°C in dark is $316\text{ }\mu\text{mol}\cdot\text{g}^{-1}\cdot\text{h}^{-1}$, close to those of the reaction carried out in the presence of the CeO₂ nanostructures ($373\text{ }\mu\text{mol}\cdot\text{g}^{-1}\cdot\text{h}^{-1}$) or the mixture of the AuNS530 and CeO₂ nanostructure ($376\text{ }\mu\text{mol}\cdot\text{g}^{-1}\cdot\text{h}^{-1}$) under the Xe lamp (Supporting Information Table S3). These results suggest that the oxidation of benzyl alcohol over the CeO₂ nanostructures and the mixture of the AuNS530 and CeO₂ nanostructures under the Xe lamp is mainly driven thermally due to the high light flux of the lamp. Therefore, the catalytic activity of the (AuNS591 core)@CeO₂ nanostructures under the 671 nm laser is contributed by both plasmonic photothermal conversion and plasmon-excitation-induced hot electrons. The Au nanocrystal cores are responsible for light absorption to trigger the catalytic activity of the CeO₂ shell. The contribution of the hot-electron effect is estimated to be $\sim 53\%$ by subtracting the conversion yield of the reaction performed in the dark from that obtained under the laser because the temperatures of the reaction solution under the two conditions are the same. Our catalytic reaction study demonstrates clearly that the LSPR of the Au nanocrystal core plays an essential role in enhancing the catalytic activity of the CeO₂ shell.

The oxidation of benzyl alcohol over noble metals supported on metal oxides under heating conditions has been investigated before.^{32,47,48} In our study, we focus on the plasmonic effect, which involves both photothermal conversion and hot-electron injection. The heating effect resulting from plasmonic photothermal conversion is straightforward to understand. To further verify the hot-electron effect, open-circuit

voltages (V_{oc}) were measured on the working electrodes fabricated from the (AuNS591 core)@CeO₂ shell and pure CeO₂ nanostructures in an electrochemical cell under the 671 nm laser illumination. V_{oc} measurements can reveal subtle variations of the chemical potential on the electrode surface. The impact of the plasmon excitation was uncovered by turning on and off the laser illumination alternately during the V_{oc} measurements. As shown in Figure 6d, despite a background that increases over time, the laser illumination unambiguously increases V_{oc} by $\sim 2\text{ mV}$. This increase in V_{oc} vanishes once the laser light is turned off. The V_{oc} increase is correlated to the increase of the chemical potential of the sample surface. Intuitively, an electrode surface with an increased Fermi level requires a more positive potential to keep electrons from jumping out across the surface into the electrolyte. The rising background can be attributed to a gradual reduction of the sample surface when the electrode is relocated from ambient air that has a lower chemical potential to nitrogen-bubbled 0.1 M KOH solution that has a higher chemical potential. The background is believed to flatten out when the chemical potentials of the sample and the electrolyte reach an equilibrium. To understand the increase in the Fermi level of the (Au nanosphere core)@CeO₂ nanostructure electrode, the band alignment diagram between Au and CeO₂ is drawn in Figure S19 of the Supporting Information. CeO₂ under ambient condition is generally thought of being an n-type semiconductor due to O vacancies. Once Au and CeO₂ are in contact, a Schottky junction forms at the Au–CeO₂ interface, with the conduction and valence bands bending upward toward the interface at the CeO₂ side. When incoming photons excite the LSPR of the Au nanocrystal core, the decay of the plasmon transfers energy to electrons. When some electrons gain enough kinetic energy, or in other words become “hot” enough,^{16,19} they can have a probability to overcome the Schottky barrier and inject into the conduction band of CeO₂. Accumulation of the electrons injected into CeO₂ increases its chemical potential. In our case, the Au nanocrystal is the core, while CeO₂ as the shell is exposed to the electrolyte. Under the 671 nm laser illumination, the chemical potential increase of the CeO₂ shell results in an increase in V_{oc} . For the working electrode made of the pure CeO₂ nanostructures, no V_{oc} variation was observed when the laser was turned on and off, suggesting the necessities of the plasmon excitation and the Schottky junction for the electron injection into CeO₂.

The electrons injected in CeO₂ get trapped to generate Ce(III) species (Figure 7). The enrichment of Ce(III) species facilitates the catalytic oxidation of benzyl alcohol into benzaldehyde with O₂ according to the previous mechanistic studies of this reaction.^{48,49} Specifically, upon the adsorption of O₂ on the surface

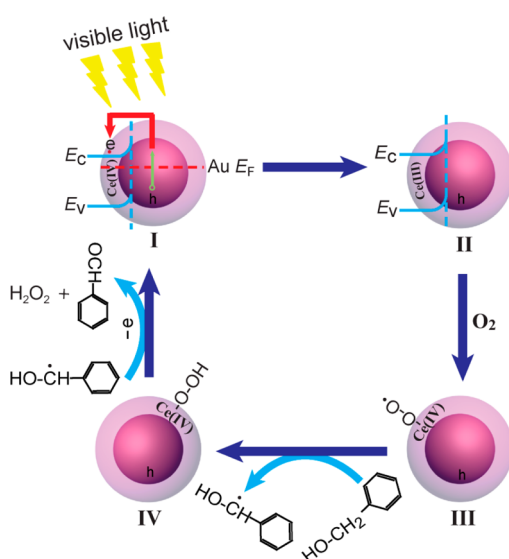


Figure 7. Proposed mechanism for the selective oxidation of benzyl alcohol to benzaldehyde with O_2 over the (Au core)@(CeO₂ shell) nanostructure catalyst under visible light illumination.

of the CeO₂ shell and coordination to the oxygen-deficient Ce(III) sites, Ce-coordinated superoxide species, Ce(IV)–O–O[•], are formed. These superoxide species evolve into cerium hydroperoxide by abstraction of α -H from the –CH₂– group of benzyl alcohol. Cerium hydroperoxide can then combine with a proton from the dehydrogenated species to produce H₂O₂, yielding benzaldehyde as the product, and an

electron is simultaneously transferred to the Au nanocrystal core to recover the charge balance.

CONCLUSION

We have developed a versatile approach for coating CeO₂ on monometallic Au and bimetallic Au@Pt, Au@Pd nanocrystals to produce multifunctional core@shell nanostructures. Monodisperse (Au core)@(CeO₂ shell) nanostructures with different CeO₂ shell thicknesses and plasmon wavelengths from the visible to near-infrared region are obtained. The plasmon shifts of the (Au core)@(CeO₂ shell) nanostructures resulting from the reversible switching between the Ce(IV) and Ce(III) states are observed. The calcined (Au core)@(CeO₂ shell) nanostructures display high photocatalytic activities toward the oxidation of benzyl alcohol to benzaldehyde under the illumination of both broadband and monochromatic visible light. The enhanced photocatalytic activities are attributed to the synergistic effect between the Au nanocrystal core acting as a plasmonic component for efficient light harvesting and the CeO₂ shell providing catalytically active sites for the oxidation reaction. The (Au core)@(CeO₂ shell) nanostructure allows the light energy harvested by the Au nanocrystal core to be effectively transferred to the catalytic CeO₂ shell. Moreover, our (Au core)@(CeO₂ shell) nanostructures will also be of interest for applications in plasmon regulation, gas sensing, solar energy harvesting, and biomedical antioxidant therapy.

METHODS

All of the core@shell nanostructure preparations were carried out in aqueous solutions with deionized water as the solvent.

Preparation of the (Au Nanosphere Core)@(CeO₂ Shell) Nanostructures. The two Au nanosphere samples were purchased from Nano-Seedz and employed as the cores. They were dispersed in aqueous solutions and stabilized with CTAB. Before CeO₂ coating, the concentrated Au nanosphere solution (2.0 mL, particle concentration: AuNS530, 4.92×10^{11} particles·mL⁻¹; AuNS591, 8.4×10^{10} particles·mL⁻¹) was redispersed into a CTAB solution (20 mL, 0.025 M). An EDTA–NH₃ mixture solution was prepared by adding concentrated ammonia (0.38 mL, 30 wt %) in water (40 mL), followed by the dissolution of EDTA (0.4 mmol). This mixture solution was used for all of the CeO₂ coating experiments. For the preparation of (Au nanosphere core)@(CeO₂ shell) nanostructures, the EDTA–NH₃ solution (3.0 mL) and a Ce(NO₃)₃ solution (0.3 mL, 0.1 M, prepared from Ce(NO₃)₃·6H₂O) were sequentially added into the Au nanosphere solution. The final coating solution was mixed by repeated gentle inversion for 1 min and then kept in an oven at 90 °C for 5 h. The resultant core@shell nanostructure product was centrifuged at 5000g for 10 min. The precipitate was redispersed into water (2 mL) for further use.

Preparation of the (Au Nanorod Core)@(CeO₂ Shell) Nanostructures. Four (Au nanorod core)@(CeO₂ shell) nanostructure samples were synthesized using four Au nanorod samples with different longitudinal plasmon wavelengths. They were grown with CTAB as the stabilizing agent following a seed-mediated method.^{50,51} For the preparation of the (Au nanorod core)@(CeO₂ shell) nanostructures, the as-grown Au nanorod solution (10 mL, $(3 \pm 2) \times 10^{10}$ particles·mL⁻¹) was centrifuged and then

redispersed into a CTAB solution (8 mL, 0.025 M). The EDTA–NH₃ solution (1.4 mL) and Ce(NO₃)₃ solution (0.14 mL, 0.1 M) were sequentially added into the Au nanorod solution. The obtained solution was mixed by repeated gentle inversion for 1 min and then kept in an oven at 90 °C for 5 h. The resultant nanostructure product was centrifuged at 4000g for 10 min. The precipitate was redispersed into water (1 mL) for further use. The (Au nanorod core)@(CeO₂ shell) nanostructure samples with different shell thicknesses were made similarly by changing the reaction time from 1 to 8 h or the volume of the Ce(NO₃)₃ solution from 0.08 to 0.16 mL.

Preparation of the (Au Nanorod Core)@(Pd Shell)@(CeO₂ Shell) and (Au Nanorod Core)@(Pt Shell)@(CeO₂ Shell) Nanostructures. The bimetallic Au@Pd and Au@Pt nanorods were first prepared according to our reported procedures.⁵² Specifically, for the preparation of the (Au nanorod core)@(Pd shell) nanostructure sample, the centrifuged AuNR715 sample (10 mL, 1×10^{10} particles·mL⁻¹) was added into a growth solution composed of CTAB (40 mL, 0.025 M), H₂PdCl₄ (0.3 mL, 0.01 M), and ascorbic acid (0.15 mL, 0.1 M). The obtained solution was mixed by gentle inversion for 10 s and then kept at room temperature for 6 h. The (Au nanorod core)@(Pt shell) nanostructure sample was made by adding the centrifuged AuNR715 sample (10 mL, 1×10^{10} particles·mL⁻¹) into a growth solution composed of CTAB (40 mL, 0.025 M), H₂PtCl₆ (0.3 mL, 0.01 M), and ascorbic acid (0.3 mL, 0.1 M). The obtained solution was mixed by gentle inversion for 10 s and then kept in an oven at 80 °C for 6 h. The preparations of the (Au nanorod core)@(Pd shell)@(CeO₂ shell) and (Au nanorod core)@(Pt shell)@(CeO₂ shell) nanostructure samples were similar to that for the (Au nanorod core)@(CeO₂ shell) nanostructure samples, except that the Au nanorod

sample was replaced with the (Au nanorod core)@(Pd shell) or (Au nanorod core)@(Pt shell) nanostructure sample.

Removal of CTAB from the (Au Core)@(CeO₂ Shell) Nanostructures. For the photocatalytic reaction, the (AuNS530 core)@(CeO₂ shell), (AuNS591 core)@(CeO₂ shell), and (AuNR715 core)@(CeO₂ shell) nanostructure samples were calcined to remove CTAB molecules that were adsorbed in the CeO₂ shell. Specifically, the as-prepared core@shell nanostructure sample was washed and transferred with absolute alcohol (1 mL) into a Pyrex test tube having an inner diameter of 1.5 cm and a length of 12 cm. After absolute alcohol was completely evaporated at 80 °C in a muffle furnace, the sample in the test tube was then calcined at 350 °C for 3 h in the furnace. Finally, the calcined core@shell nanostructure sample was redispersed into acetonitrile (2 mL) by ultrasonication for the photocatalytic reaction. After calcination, the plasmon resonance wavelength, morphology, and dispersibility of the nanostructure sample remained nearly unchanged.

Plasmonic Sensing of the Oxidation State of Ce in the Shell. The plasmon shifts induced by the redox reaction of the CeO₂ shell were examined with the (AuNR715 core)@(CeO₂ shell) nanostructure sample. The as-prepared nanostructure sample (10 mL) was centrifuged and redispersed in water (10 mL). The resultant nanostructure solution (1 mL) was diluted into water (2 mL) in a cuvette. To reduce the shell, NaBH₄ (0.1 mL, 0.1 M) was added into the nanostructure solution. The extinction spectra were then recorded to monitor the plasmon shift as a function of time. After the reduction-induced plasmon shift was completed, H₂O₂ (0.1 mL, 1.0 M) was added into the nanostructure solution to oxidize the shell. The oxidation-induced plasmon shift was monitored again by the extinction measurements.

Photocatalytic Selective Oxidation of Benzyl Alcohol in Acetonitrile under Broad-Band Light ($\lambda > 420$ nm) from a Xe Lamp. A continuous Xe lamp (CHF-XM500, Beijing Trusttech Technology Co., Ltd.) equipped with a 420 nm long-pass filter was utilized as the broad-band light source for illumination. The electric power of the lamp was set at 250 W, at which the light intensity was 5.6 W. The photocatalytic reactions with the different nanostructure catalysts were carried out in a transparent Pyrex test tube having an inner diameter of 1.5 cm and a length of 12 cm. The nanostructure catalyst was dispersed in acetonitrile (2 mL), followed by the injection of benzyl alcohol into the suspension. After the solution was bubbled with O₂ for 30 min, the test tube was sealed with a balloon that was full of O₂ at a pressure of ~1 atm. The reaction mixture was kept under the illumination of the Xe lamp with a focused spot size of 3.1 cm². After a certain period of time, the reaction solution was centrifuged at 10 000g for 20 min to remove the nanostructure catalyst. The amounts of benzyl alcohol, benzaldehyde, and other byproducts in the solution were determined on a high-performance liquid chromatography system (Waters 625 LC) equipped with a Waters 600 controller, a Waters 486 tunable absorbance detector, and a C18 (250 mm × 4.6 mm, 4 μ m particle size) analytical column (ACE-119 ACE-121). The mobile phase consisted of a mixture of acetic acid solution (5 mM, pH = 3.76) and acetonitrile at 65:35 (v/v). During the measurements, 15 μ L of the diluted sample was injected into the analytical column at a flow rate of 1.0 mL·min⁻¹ and monitored with a UV detector at 258 nm.

Photocatalytic Reaction under the Illumination of a Monochromatic 671 nm Laser. A continuous semiconductor laser diode (SDL-671-3200MFL, Shanghai Dream Lasers Technology Co., Ltd.) at 671 nm was utilized as the monochromatic light source. The light intensity was fixed at 1.1 W, except for the power-dependence experiment. The laser spot size on the reaction tube was 1.8 cm². The selective oxidation of benzyl alcohol in acetonitrile with the nanostructure catalysts was carried out in a similar way to that under the broad-band light source.

Open-Circuit Voltage Measurements. The working electrode was prepared with the (AuNS591 core)@(CeO₂ shell) nanostructure sample or the CeO₂ nanostructure sample. Specifically, the as-prepared (AuNS591 core)@(CeO₂ shell) nanostructure sample (10 mL) or the CeO₂ nanostructure sample (10 mL) was centrifuged and redispersed in ethanol (2 mL). One hundred microliters of the concentrated suspension was drop-cast on the conducting surface of a transparent indium–tin oxide (ITO)

glass slide of 1 cm × 5 cm in area. The electrode was first heated at 65 °C for 1 h to evaporate ethanol and then calcined at 350 °C for 3 h to increase the adhesion among the nanostructures or nanoparticles. Ag/AgCl was used as the reference electrode and a Pt plate as the counter electrode. KOH (0.1 M) was bubbled with N₂ for 1 h and then used as the electrolyte. The measurements were carried out on an electrochemical workstation (CHI 760E). Once assembled, the electrochemical cell was set still for 0.5 h at open circuit without disturbance so that the cell could reach an equilibrium. After that, the open-circuit voltage was recorded continuously for 20 min, during which the working electrode was illuminated with a laser beam (671 nm, 1.1 W) at a spot size of 0.4 cm². The laser beam was chopped on and off at an interval of 100 s.

Characterization. SEM imaging was performed on an FEI Quantum 400F microscope operated at 20 kV. Low-magnification TEM imaging was performed on an FEI Tecnai Spirit microscope at 120 kV. HRTEM imaging, STEM characterization, and elemental mapping were carried out on an FEI Tecnai F20 microscope operated at 200 kV. Extinction spectra were taken on a Hitachi U-3501 UV/visible/NIR spectrophotometer with 1.0 cm quartz cuvettes. The XRD patterns were acquired on a Rigaku Smartlab diffractometer with Cu K α radiation. ICP-OES measurements were performed on a PerkinElmer Optima 4300DV system. XPS spectra were measured on a Quantum 2000 X-ray photoelectron spectrometer equipped with an Al K α ($h\nu = 1486.6$ eV) radiation source. For the XPS measurements, each nanostructure sample was washed by centrifugation twice and finally concentrated into water (0.5 mL). The concentrated sample was drop-cast on a clean glass slide to form a uniform film after being dried in a vacuum oven. The operating pressure during the XPS measurements was approximately 5×10^{-6} Pa. The Raman spectra were collected using a RM-1000 micro-Raman spectrometer under excitation at 514 nm.

Conflict of Interest: The authors declare no competing financial interest.

Acknowledgment. This work was supported by Hong Kong RGC GRF (Ref. No. CUHK403312, Project Code 2130320) and NNSFC (Ref. No. 21229101).

Supporting Information Available: Synthesis details, extinction spectra, and TEM images of the CeO₂ nanostructures and silica-coated Au nanocrystals; extinction spectra and TEM images of the ceria-coated Au nanospheres, Au nanorods, and bimetallic Au@Pt nanocrystals; effects of the coating time, Ce(NO₃)₃ amount, Ce³⁺/EDTA molar ratio, and ammonia amount on the coating process; HRTEM images and elemental mapping of the ceria-coated bimetallic Au@Pd and Au@Pt nanocrystals; extinction spectra of the (Au nanorod core)@(CeO₂ shell) nanostructures and the uncoated Au nanorods under the different redox conditions; XPS spectra of the core@shell nanostructures under the different redox conditions; Raman spectra of the core@shell nanostructures; emission spectrum of the Xe lamp; time-dependent production of benzaldehyde; extinction spectra and TEM images of the recycled (Au core)@(CeO₂ shell) nanostructures; schematics of the relative band alignment and Schottky junction; fitted binding energies and area fractions; masses of the different catalysts; catalytic conversion rates and percentages under the Xe lamp and laser light; catalytic conversion rates obtained in previous related studies; solution temperatures under the photocatalytic reaction conditions. This material is available free of charge via the Internet at <http://pubs.acs.org>.

REFERENCES AND NOTES

1. Chueh, W. C.; Falter, C.; Abbott, M.; Scipio, D.; Furler, P.; Haile, S. M.; Steinfeld, A. High-Flux Solar-Driven Thermochemical Dissociation of CO₂ and H₂O Using Nonstoichiometric Ceria. *Science* **2010**, *330*, 1797–1801.
2. Zhou, H.-P.; Wu, H.-S.; Shen, J.; Yin, A.-X.; Sun, L.-D.; Yan, C.-H. Thermally Stable Pt/CeO₂ Hetero-nanocomposites with High Catalytic Activity. *J. Am. Chem. Soc.* **2010**, *132*, 4998–4999.

3. Cagnello, M.; Delgado Jaén, J. J.; Hernández Garrido, J. C.; Bakhmutsky, K.; Montini, T.; Calvino Gámez, J. J.; Gorte, R. J.; Fornasiero, P. Exceptional Activity for Methane Combustion over Modular Pd@CeO₂ Subunits on Functionalized Al₂O₃. *Science* **2012**, *337*, 713–717.
4. Joy, N. A.; Rogers, P. H.; Nandasiri, M. I.; Thevuthasan, S.; Carpenter, M. A. Plasmonic-Based Sensing Using an Array of Au–Metal Oxide Thin Films. *Anal. Chem.* **2012**, *84*, 10437–10444.
5. Joy, N. A.; Nandasiri, M. I.; Rogers, P. H.; Jiang, W. L.; Varga, T.; Kuchibhatla, S. V. N. T.; Thevuthasan, S.; Carpenter, M. A. Selective Plasmonic Gas Sensing: H₂, NO₂, and CO Spectral Discrimination by a Single Au–CeO₂ Nanocomposite Film. *Anal. Chem.* **2012**, *84*, 5025–5034.
6. Esposito, V.; Traversa, E. Design of Electroceramics for Solid Oxides Fuel Cell Applications: Playing with Ceria. *J. Am. Ceram. Soc.* **2008**, *91*, 1037–1051.
7. Corma, A.; Atienzar, P.; García, H.; Chane-Ching, J.-Y. Hierarchically Mesostructured Doped CeO₂ with Potential for Solar-Cell Use. *Nat. Mater.* **2004**, *3*, 394–397.
8. Pagliari, F.; Mandoli, C.; Forte, G.; Magnani, E.; Pagliari, S.; Nardone, G.; Licoccia, S.; Minieri, M.; Nardo, P. D.; Traversa, E. Cerium Oxide Nanoparticles Protect Cardiac Progenitor Cells from Oxidative Stress. *ACS Nano* **2012**, *6*, 3767–3775.
9. Uchiyama, T.; Yoshida, H.; Kuwauchi, Y.; Ichikawa, S.; Shimada, S.; Haruta, M.; Takeda, S. Systematic Morphology Changes of Gold Nanoparticles Supported on CeO₂ during CO Oxidation. *Angew. Chem., Int. Ed.* **2011**, *50*, 10157–10161.
10. Si, R.; Flytzani-Stephanopoulos, M. Shape and Crystal-Plane Effects of Nanoscale Ceria on the Activity of Au–CeO₂ Catalysts for the Water–Gas Shift Reaction. *Angew. Chem., Int. Ed.* **2008**, *47*, 2884–2887.
11. Bruix, A.; Rodríguez, J.; Ramírez, P. J.; Senanayake, S. D.; Evans, J.; Park, J. B.; Stacchiola, D.; Liu, P.; Hrbek, J.; Illas, F. A New Type of Strong Metal–Support Interaction and the Production of H₂ through the Transformation of Water on Pt/CeO₂(111) and Pt/CeO_x/TiO₂(110) Catalysts. *J. Am. Chem. Soc.* **2012**, *134*, 8968–8974.
12. Hwang, J.-H.; Mason, T. O. Defect Chemistry and Transport Properties of Nanocrystalline Cerium Oxide. *Z. Phys. Chem.* **1998**, *207*, 21–38.
13. Ravelli, D.; Dondi, D.; Fagnoni, M.; Albini, A. Photocatalysis. A Multi-faceted Concept for Green Chemistry. *Chem. Soc. Rev.* **2009**, *38*, 1999–2011.
14. Linic, S.; Christopher, P.; Ingram, D. B. Plasmonic-Metal Nanostructures for Efficient Conversion of Solar to Chemical Energy. *Nat. Mater.* **2011**, *10*, 911–921.
15. Tong, H.; Ouyang, S. X.; Bi, Y. P.; Umezawa, N.; Oshikiri, M.; Ye, J. H. Nano-photocatalytic Materials: Possibilities and Challenges. *Adv. Mater.* **2012**, *24*, 229–251.
16. Xiao, M. D.; Jiang, R. B.; Wang, F.; Fang, C. H.; Wang, J. F.; Yu, J. C. Plasmon-Enhanced Chemical Reactions. *J. Mater. Chem. A* **2013**, *1*, 5790–5805.
17. Wang, F.; Li, C. H.; Chen, H. J.; Jiang, R. B.; Sun, L.-D.; Li, Q.; Wang, J. F.; Yu, J. C.; Yan, C.-H. Plasmonic Harvesting of Light Energy for Suzuki Coupling Reactions. *J. Am. Chem. Soc.* **2013**, *135*, 5588–5601.
18. Sarina, S.; Zhu, H. Y.; Jaatinen, E.; Xiao, Q.; Liu, H. W.; Jia, J. F.; Chen, C.; Zhao, J. Enhancing Catalytic Performance of Palladium in Gold and Palladium Alloy Nanoparticles for Organic Synthesis Reactions through Visible Light Irradiation at Ambient Temperatures. *J. Am. Chem. Soc.* **2013**, *135*, 5793–5801.
19. Mukherjee, S.; Libisch, F.; Large, N.; Neumann, O.; Brown, L. V.; Cheng, J.; Lassiter, J. B.; Carter, E. A.; Nordlander, P.; Halas, N. J. Hot Electrons Do the Impossible: Plasmon-Induced Dissociation of H₂ on Au. *Nano Lett.* **2013**, *13*, 240–247.
20. Jiang, R. B.; Li, B. X.; Fang, C. H.; Wang, J. F. Metal/Semiconductor Hybrid Nanostructures for Plasmon-Enhanced Applications. *Adv. Mater.* **2014**, *10.1002/adma.201400203*.
21. Gao, H. W.; Liu, C.; Jeong, H. E.; Yang, P. D. Plasmon-Enhanced Photocatalytic Activity of Iron Oxide on Gold Nanopillars. *ACS Nano* **2012**, *6*, 234–240.
22. Tsukamoto, D.; Shiraishi, Y.; Sugano, Y.; Ichikawa, S.; Tanaka, S.; Hirai, T. Gold Nanoparticles Loaded at the Interface of Anatase/Rutile TiO₂ Particles as Active Plasmonic Photocatalysts for Aerobic Oxidation. *J. Am. Chem. Soc.* **2012**, *134*, 6309–6315.
23. Tanaka, A.; Hashimoto, K.; Kominami, H. Preparation of Au/CeO₂ Exhibiting Strong Surface Plasmon Resonance Effective for Selective or Chemoselective Oxidation of Alcohols to Aldehydes or Ketones in Aqueous Suspensions under Irradiation by Green Light. *J. Am. Chem. Soc.* **2012**, *134*, 14526–14533.
24. Liu, L. Q.; Ouyang, S. X.; Ye, J. H. Gold-Nanorod-Photosensitized Titanium Dioxide with Wide-Range Visible-Light Harvesting Based on Localized Surface Plasmon Resonance. *Angew. Chem., Int. Ed.* **2013**, *52*, 6689–6693.
25. Mubeen, S.; Lee, J.; Singh, N.; Krämer, S.; Stucky, G. D.; Moskovits, M. An Autonomous Photosynthetic Device in which All Charge Carries Derive from Surface Plasmons. *Nat. Nanotechnol.* **2013**, *8*, 247–251.
26. Kominami, H.; Tanaka, A.; Hashimoto, K. Mineralization of Organic Acids in Aqueous Suspensions of Gold Nanoparticles Supported on Cerium(IV) Oxide Powder under Visible Light Irradiation. *Chem. Commun.* **2010**, *46*, 1287–1289.
27. Kominami, H.; Tanaka, A.; Hashimoto, K. Gold Nanoparticles Supported on Cerium(IV) Oxide Powder for Mineralization of Organic Acids in Aqueous Suspensions under Irradiation of Visible Light of $\lambda = 530$ nm. *Appl. Catal., A* **2011**, *397*, 121–126.
28. Primo, A.; Marino, T.; Corma, A.; Molinari, R.; García, H. Efficient Visible-Light Photocatalytic Water Splitting by Minute Amounts of Gold Supported on Nanoparticulate CeO₂ Obtained by a Biopolymer Templating Method. *J. Am. Chem. Soc.* **2011**, *133*, 6930–6933.
29. Kuo, C.-H.; Yang, Y.-C.; Gwo, S.; Huang, M. H. Facet-Dependent and Au Nanocrystal-Enhanced Electrical and Photocatalytic Properties of Au–Cu₂O Core–Shell Heterostructures. *J. Am. Chem. Soc.* **2011**, *133*, 1052–1057.
30. Kong, L. N.; Chen, W.; Ma, D. K.; Yang, Y.; Liu, S. S.; Huang, S. M. Size Control of Au@Cu₂O Octahedra for Excellent Photocatalytic Performance. *J. Mater. Chem.* **2012**, *22*, 719–724.
31. Liu, S. H.; Bai, S.-Q.; Zheng, Y. G.; Shah, K. W.; Han, M.-Y. Composite Metal–Oxide Nanocatalysts. *ChemCatChem* **2012**, *4*, 1462–1485.
32. Mallat, T.; Baiker, A. Oxidation of Alcohols with Molecular Oxygen on Solid Catalysts. *Chem. Rev.* **2004**, *104*, 3037–3058.
33. Luo, F.; Jia, C.-J.; Song, W.; You, L.-P.; Yan, C.-H. Chelating Ligand-Mediated Crystal Growth of Cerium Orthovanadate. *Cryst. Growth Des.* **2005**, *5*, 137–142.
34. Chen, H. J.; Shao, L.; Li, Q.; Wang, J. F. Gold Nanorods and Their Plasmonic Properties. *Chem. Soc. Rev.* **2013**, *42*, 2679–2724.
35. Yu, T.; Lim, B.; Xia, Y. N. Aqueous-Phase Synthesis of Single-Crystal Ceria Nanosheets. *Angew. Chem., Int. Ed.* **2010**, *49*, 4484–4487.
36. Zhen, J. M.; Wang, X.; Liu, D. P.; Song, S. Y.; Wang, Z.; Wang, Y. H.; Li, J. Q.; Wang, F.; Zhang, H. J. Co₃O₄@CeO₂ Core@Shell Cubes: Designed Synthesis and Optimization of Catalytic Properties. *Chem.—Eur. J.* **2014**, *20*, 4469–4473.
37. Chen, H. J.; Kou, X. S.; Yang, Z.; Ni, W. H.; Wang, J. F. Shape- and Size-Dependent Refractive Index Sensitivity of Gold Nanoparticles. *Langmuir* **2008**, *24*, 5233–5237.
38. Paier, J.; Penschke, C.; Sauer, J. Oxygen Defects and Surface Chemistry of Ceria: Quantum Chemical Studies Compared to Experiment. *Chem. Rev.* **2013**, *113*, 3949–3985.
39. Wu, Z. L.; Li, M. J.; Howe, J.; Meyer, H. M., III; Overbury, S. H. Probing Defect Sites on CeO₂ Nanoparticles with Well-Defined Surface Planes by Raman Spectroscopy and O₂ Adsorption. *Langmuir* **2010**, *26*, 16595–16606.
40. Gao, P.; Kang, Z. C.; Fu, W. Y.; Wang, W. L.; Bai, X. D.; Wang, E. G. Electrically Driven Redox Process in Cerium Oxides. *J. Am. Chem. Soc.* **2010**, *132*, 4197–4201.

41. Larachi, F.; Pierre, J.; Adnot, A.; Bernis, A. Ce 3d XPS Study of Composite $\text{Ce}_x\text{Mn}_{1-x}\text{O}_{2-y}$ Wet Oxidation Catalysts. *Appl. Surf. Sci.* **2002**, *195*, 236–250.
42. Zhang, F.; Wang, P.; Koberstein, J.; Khalid, S.; Chan, S.-W. Cerium Oxidation State in Ceria Nanoparticles Studied with X-ray Photoelectron Spectroscopy and Absorption Near Edge Spectroscopy. *Surf. Sci.* **2004**, *563*, 74–82.
43. Murugan, B.; Ramaswamy, A. V. Defect-Site Promoted Surface Reorganization in Nanocrystalline Ceria for the Low-Temperature Activation of Ethylbenzene. *J. Am. Chem. Soc.* **2007**, *129*, 3062–3063.
44. Weber, W. H.; Hass, K. C.; McBride, J. R. Raman Study of CeO_2 : Second-Order Scattering, Lattice Dynamics, and Particle-Size Effects. *Phys. Rev. B* **1993**, *48*, 178–185.
45. Dowding, J. M.; Das, S.; Kumar, A.; Dosani, T.; McCormack, R.; Gupta, A.; Sayle, T. X. T.; Sayle, D. C.; von Kalm, L.; Seal, S.; Self, W. T. Cellular Interaction and Toxicity Depend on Physicochemical Properties and Surface Modification of Redox-Active Nanomaterials. *ACS Nano* **2013**, *7*, 4855–4868.
46. Christopher, P.; Xin, H. L.; Marimuthu, A.; Linic, S. Singular Characteristics and Unique Chemical Bond Activation Mechanisms of Photocatalytic Reactions on Plasmonic Nanostructures. *Nat. Mater.* **2012**, *11*, 1044–1050.
47. Enache, D. I.; Edwards, J. K.; Landon, P.; Solsona-Espriu, B.; Carley, A. F.; Herzing, A. A.; Watanabe, M.; Kiely, C. J.; Knight, D. W.; Hutchings, G. J. Solvent-Free Oxidation of Primary Alcohols to Aldehydes Using Au-Pd/TiO₂ Catalysts. *Science* **2006**, *311*, 362–365.
48. Abad, A.; Concepción, P.; Corma, A.; García, H. A Collaborative Effect between Gold and a Support Induces the Selective Oxidation of Alcohols. *Angew. Chem., Int. Ed.* **2005**, *44*, 4066–4069.
49. Zhang, M.; Wang, Q.; Chen, C. C.; Zhang, L.; Ma, W. H.; Zhao, J. C. Oxygen Atom Transfer in the Photocatalytic Oxidation of Alcohols by TiO₂: Oxygen Isotope Studies. *Angew. Chem., Int. Ed.* **2009**, *48*, 6081–6084.
50. Kou, X. S.; Zhang, S. Z.; Yang, Z.; Tsung, C.-K.; Stucky, G. D.; Sun, L. D.; Wang, J. F.; Yan, C. H. Glutathione- and Cysteine-Induced Transverse Overgrowth on Gold Nanorods. *J. Am. Chem. Soc.* **2007**, *129*, 6402–6404.
51. Ni, W. H.; Kou, X. S.; Yang, Z.; Wang, J. F. Tailoring Longitudinal Surface Plasmon Wavelengths, Scattering and Absorption Cross Sections of Gold Nanorods. *ACS Nano* **2008**, *2*, 677–686.
52. Chen, H. J.; Wang, F.; Li, K.; Woo, K. C.; Wang, J. F.; Li, Q.; Sun, L.-D.; Zhang, X. X.; Lin, H.-Q.; Yan, C.-H. Plasmonic Percolation: Plasmon Manifested Dielectric-to-Metal Transition. *ACS Nano* **2012**, *6*, 7162–7171.